CHEMISTRY
A EUROPEAN JOURNAL

DOI: 10.1002/chem.200601219

Oxidation of Linear Trinuclear Ruthenium Complexes $[Ru_3(dpa)_4Cl_2]$ and $[Ru_3(dpa)_4(CN)_2]$: Synthesis, Structures, Electrochemical and Magnetic Properties

Ching-Kuo Kuo,[a] Isiah Po-Chun Liu,[b] Chen-Yu Yeh,[c] Chung-Hsien Chou,[a] Ting-Bin Tsao,[a] Gene-Hsiang Lee,[a] and Shie-Ming Peng*[a, b]

Abstract: The neutral, monocationic, and dicationic linear trinuclear ruthenium compounds $[Ru_3(dpa)_4(CN)_2]$, $[Ru_3(dpa)_4(CN)_2][BF_4]$, $[Ru_3(dpa)_4Cl_2][BF_4]$, and $[Ru_3(dpa)_4Cl_2][BF_4]_2$ (dpa = the anion of dipyridylamine) have been synthesized and characterized by various spectroscopic techniques. Cyclic voltammetric and spectroelectrochemical studies on the neutral and oxidized compounds are reported. These compounds undergo three successive metal-centered one-electron-transfer processes. X-ray structural studies reveal a symmetrical Ru_3 unit for these compounds. While the metal–metal bond lengths change only slightly, the metal–axial ligand lengths exhibit a significant decrease upon oxidation of the neutral complex. The electronic configuration of the Ru_3 unit changes as the axial chloride ligands are replaced by the stronger "π-acid" cyanide axial ligands. Magnetic measurements and ^{1}H NMR spectra indicate that $[Ru_3(dpa)_4Cl_2]$ and $[Ru_3(dpa)_4Cl_2][BF_4]_2$ are in a spin state of $S=0$ and $[Ru_3(dpa)_4Cl_2][BF_4]$, $[Ru_3(dpa)_4(CN)_2]$, and $[Ru_3(dpa)_4(CN)_2][BF_4]$ are in spin states of $S=1/2$, 1, and 3/2, respectively. These results are consistent with molecular orbital (MO) calculations.

Keywords: density functional calculations · metal–metal interactions · multiple bonds · N ligands · ruthenium

Introduction

Substantial efforts have been devoted over the past decade to the synthesis and characterization of linear multinuclear metal string complexes, since the first reports on trinuclear nickel and copper complexes.[1–3] This is due to their versatile chemical and physical properties and their potential applications in molecular metal wires. Previous studies on this new class of complexes have been focused on compounds of the first row metals. To date, a number of linear multinuclear complexes of various first row metals, $[M_3(dpa)_4X_2]$ (M = Cr,[4] Co,[7–11] Ni,[1,12] Cu;[2,3] X = uninegative anion), $[M_5(tpda)_4X_2]$ (M = Cr,[13,14] Co,[15] Ni;[15,16] tpda = the dianion of tri-α-pyridyldiamine), $[M_7(teptra)_4X_2]$ (M = Cr,[17] Ni;[18,19] teptra = the trianion of tetra-α-pyridyltriamine), and $[M_9(peptea)_4X_2]$ (M = Ni;[20] H_4peptea = penta-α-pyridyltetraamine), have been synthesized and characterized structurally. In 1996 we reported for the first time the synthesis and structures of the trinuclear complexes of the second-row metals ruthenium and rhodium.[21] Previous studies of the multinuclear complexes show that the strength of metal–metal interactions is dependent on the type and number of metal centers, the nature of the axial ligands, and the oxidation states of the complexes.[15b,16] According to theoretical calculations, the electronic configuration of the triruthenium unit in $[Ru_3(dpa)_4Cl_2]$ is described as $\sigma^2\pi^4\delta^2\pi_{nb}{}^4\delta_{nb}{}^2\delta^{*2}\sigma_{nb}{}^2$, thus resulting in the diamagnetism of the complex and a bond order of three over the Ru_3 unit; that is, a bond order of 1.5 between adjacent ruthenium ions. The HOMO σ_{nb} of $[Ru_3(dpa)_4Cl_2]$ has a mixed character of metal–metal nonbonding and metal–axial ligand antibonding orbitals. Therefore, it is expected that removal of an electron from the neu-

[a] Dr. C.-K. Kuo, Dr. C.-H. Chou, Dr. T.-B. Tsao, G.-H. Lee, Prof. S.-M. Peng
Department of Chemistry, National Taiwan University
No 1, Roosevelt Rd., Sec. 4, Taipei (Taiwan)
Fax: (+886) 2-8369-3765
E-mail: smpeng@ntu.edu.tw

[b] I. P.-C. Liu, Prof. S.-M. Peng
Institute of Chemistry, Academia Sinica
Taipei (Taiwan)

[c] Prof. C.-Y. Yeh
Department of Chemistry, National Chung Hsing University
Taichung (Taiwan)

Supporting information for this article is available on the WWW under http://www.chemeurj.org/ or from the author.

tral complex $[Ru_3(dpa)_4Cl_2]$ results in an increase in the metal–axial ligand interactions, and little effect on the metal–metal interactions. To see the influence of the oxidation states and the nature of axial ligands on the structures and metal–metal interactions of the triruthenium complexes, we decided to synthesize the neutral complex $[Ru_3(dpa)_4(CN)_2]$ with π-acid axial ligands, and the oxidized complexes of $[Ru_3(dpa)_4Cl_2]$ and $[Ru_3(dpa)_4(CN)_2]$. In this paper, we report the synthesis of neutral and oxidized triruthenium complexes, their crystal structures, their electrochemical and magnetic properties, and theoretical calculations.

Results and Discussion

In our previous report of the neutral triruthenium complex, the low-yielding procedure, the reaction of Hdpa (dipyridylamine) with $[Ru_2(OAc)_4Cl]$ in the presence of base, prevented us from further studying the oxidation chemistry of this complex. Under modified conditions, a moderate yield (53%) for the synthesis of the oxidized compound $[Ru_3(dpa)_4Cl_2][BF_4]$ (**2**) was achieved (Scheme 1). During the process of metalation, excess LiCl was used to prevent the formation of the acetate complexes, and the crude products after workup were immediately oxidized by ferrocenium tetrafluoroborate ($FcBF_4$) to suppress decomposition. The neutral form $[Ru_3(dpa)_4Cl_2]$ (**1**) was obtained by reacting compound **2** with excess hydrazine and crystallizing from CH_2Cl_2 and hexane. The two-electron oxidized compound $[Ru_3(dpa)_4Cl_2][BF_4]_2$ (**3**) was obtained by treating compound **2** with excess $NOBF_4$ in CH_2Cl_2. Crystallization of the product from CH_2Cl_2 and ether produced dark purple crystals. The compound with π-acid axial ligands, $[Ru_3(dpa)_4(CN)_2][BF_4]$ (**5**), was synthesized by reacting compound **2** with excess NaCN and crystallized from CH_2Cl_2 and hexane. The neutral form $[Ru_3(dpa)_4(CN)_2]$ (**4**) was obtained by reacting compound **5** with excess hydrazine and crystallized from CH_2Cl_2 and hexane.

Figure 1 shows the crystal structures of **2** and **3**. Some selected bond lengths and crystallographic data are listed in Tables 1 and 2, respectively. In the crystal structure of compound **2**, the Ru_3 unit is essentially symmetrical and is helically wrapped by four dpa ligands with two chloride ions as the axial ligands. The positive charge in the Ru_3 core is balanced by one BF_4^- ion. The crystal structure of compound **3** is similar to that of compound **2**, except that the two positive charges are compensated by two BF_4^- ions. In compounds **2** and **3**, the Ru–N distances lie in the range of 2.04–2.12 Å, comparable with those of compound **1**, but much longer (by about 0.1–0.2 Å) than those in the trinuclear analogues of first-row metals. The average Ru–Ru bond length of compound **2** is 2.291 Å, which is slightly longer (by 0.035 Å) than that of the neutral analogue **1**. Such an increase is more pronounced in the case of compound **3** in which the Ru–Ru separation increases by 0.058 Å relative to that of the neutral complex **1**. This can be ascribed to the increased repulsive forces between the adjacent ruthenium atoms as the oxidation state increases. Although there are slight changes to the Ru–Ru distances upon one- and two-electron oxidation, the bond order of three over the Ru_3 unit remains unchanged. It should be noted that the Ru_3 units in **1**, **2**, and **3** are not in a linear arrangement, which has not been seen previously in the trinuclear compounds of first-row metals. The reasons for the nonlinear arrangement of the Ru_3 units are still unclear. Preliminary theoretical calculations show that the deviation causes a decrease in the energy of the HOMO orbital. The most striking feature in these triruthenium compounds is that the average Ru–Cl distance exhibits a significant change as the Ru_3 core is oxidized. The Ru–Cl bond lengths are 2.596, 2.466, and 2.407 Å for **1**, **2**, and **3**, respectively. The significant decrease in the Ru–Cl distances and a slight change in the Ru–Ru bond lengths upon oxidation are consistent with the metal–metal nonbonding and metal–axial ligand antibonding character of the HOMO orbital. Figure 2 shows the crystal structures of **4** and **5**. Some selected bond lengths and crystallographic data are also listed in Tables 1 and 2, respectively. The crystal structure of **4** is similar to that of **1** except that the chlo-

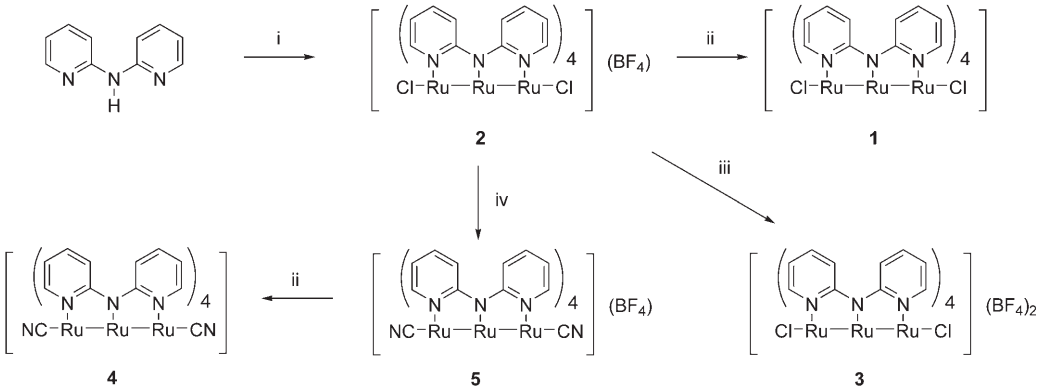

Scheme 1. Reagents and conditions: i) $[Ru_2(OAc)_4Cl]$, LiCl, *t*BuOK/*n*BuOH, naphthalene, reflux, 2 h; then add $Fc[BF_4]$, 53%; ii) hydrazine, CH_2Cl_2, 10 min, 63%; iii) $NOBF_4$, CH_2Cl_2, 3 h, 50%; iv) NaCN, CH_3CN, 6 h, 80%.

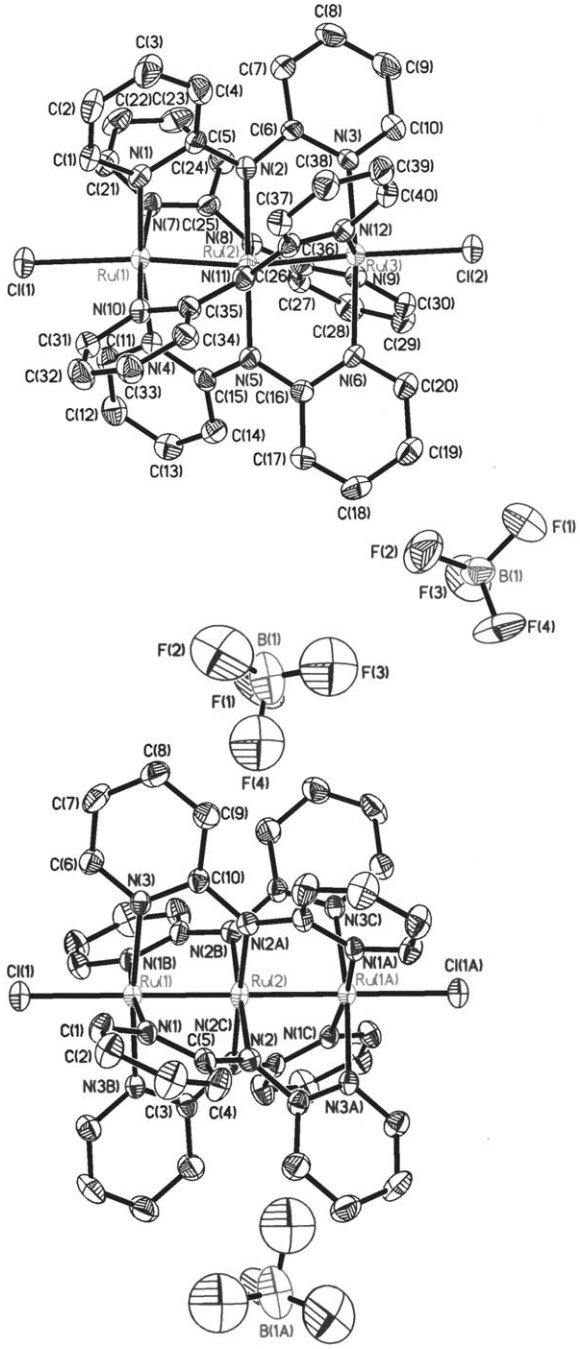

Figure 1. Crystal structures of **2** (top) and **3** (bottom). Atoms are drawn at the 30% probability level and hydrogen atoms are omitted for clarity.

ride ions are replaced by cyanide groups. The average Ru–Ru bond lengths of compounds **4** and **5** are 2.377 and 2.347 Å, respectively. These are longer than those of the chloride-substituted Ru_3 unit, because the bond order between adjacent ruthenium ions decreases from 1.5 to 1 in the neutral complexes, as will be discussed below. The Ru–C bond lengths (2.053(5) and 2.061(5) Å) and the C≡N bond lengths (1.108(7) and 1.126(6) Å) in **4** are comparable to those in the monoruthenium dicyano adducts[22] and diruthenium dicyano adducts.[23] The C≡N bond lengths (1.018(7) and 1.028(6) Å) in compound **5** are shorter than those in the neutral complex **4**. This may be ascribed to the effect of the thermal vibrations of carbon and nitrogen atoms. The bond order between adjacent ruthenium ions increases from 1 to 1.25 as one electron is removed from the neutral complex. The average Ru–Ru bond length of **5** is shorter than that of **4** by about 0.030 Å, whereas the average Ru–C distance is longer by about 0.035 Å.

It is known that ruthenium complexes have various oxidation states. Thus, a rich redox chemistry for our triruthenium compounds is expected and it is desirable to study the electrochemical properties of these compounds. Figure 3 shows the cyclic voltammograms of compounds **2** and **5** in CH_2Cl_2 containing 0.1 M tetra-*n*-butylammonium perchlorate (TBAP). Compound **2** shows three well-defined redox couples at +0.07, +0.89, and +1.53 V, corresponding to $[Ru_3(dpa)_4Cl_2]^+/[Ru_3(dpa)_4Cl_2]$, $[Ru_3(dpa)_4Cl_2]^{2+}/[Ru_3(dpa)_4Cl_2]^+$, and $[Ru_3(dpa)_4Cl_2]^{3+}/[Ru_3(dpa)_4Cl_2]^{2+}$, respectively. Three successive redox couples of compounds **1** and **3** are observed at potentials identical to those of compound **2**. In the case of $[Ru_3(dpa)_4(CN)_2]$, two well-defined redox couples at −0.06 and +0.93 V, corresponding to $[Ru_3(dpa)_4(CN)_2]^+/[Ru_3(dpa)_4(CN)_2]$ and $[Ru_3(dpa)_4(CN)_2]^{2+}/[Ru_3(dpa)_4(CN)_2]^+$, respectively, are observed. The third oxidation, occurring at about +1.63 V, is irreversible. Similarly, the electrochemical properties of compound **4** resemble those of compound **5**.

To see the stability of these reduced and oxidized forms spectroelectrochemistry was performed at various applied potentials. Spectral changes were observed in compound **2** when the applied potential was varied from +0.15 to −0.10 V in CH_2Cl_2 containing 0.1 M TBAP (Figure S1 in the Supporting Information). The peaks at 270, 476, 536, and 922 nm decrease, whereas those at 262, 342, and 476 nm increase. The resulting spectrum is similar to that of the neutral complex **1** obtained by the chemical method. The second and third oxidation reactions were also investigated by spectroelectrochemistry as shown in Figure S1 in the Supporting Information. At an applied potential of +0.98 V, the resulting spectrum shows peaks at 280, 492, 544, and 1052 nm, which are identical with those of compound **3**. Further oxidation at +1.63 V leads to significant spectral changes with peaks at 262, 528, and 1420 nm. There are clear isosbestic points during each step of the electrochemical reactions indicating that no intermediates or by-products are produced. All these electrochemical reactions are reversible on the spectroelectrochemical timescale (about 30 min). The spectroelectrochemical behavior of compound **3** resembles that of compound **2**. In the electronic absorption spectra, the oxidized complexes exhibit broad bands at wavelengths longer than 800 nm, whereas no bands in the near infrared (NIR) range are present for the neutral form. These broad bands can be ascribed to the intervalence charge transfer in the mixed valence compounds **2** and **3**. The spectroelectrochemical behaviors of the dicyanide-substituted compounds resemble those of the dichloride-substituted analogues. The dicyanide compounds exhibit a broad

Table 1. Selected bond lengths [Å] and angles [°] for **1**–**5**.

	1[a]	**2**	**3**	**4**	**5**
Ru(1)−Cl	2.596(2)	2.4656(13)	2.407(2)		
Ru(3)−Cl	2.596(2)	2.4656(13)	2.407(2)		
Ru(1)−C				2.053(5)	2.092(5)
Ru(3)−C				2.061(5)	2.091(5)
Ru(1)−Ru(2)[b]	2.2537(5)	2.2939(6)	2.3117(10)	2.3738(5)	2.3447(4)
Ru(2)−Ru(3)[b]	2.2537(5)	2.2882(6)	2.3117(10)	2.3794(5)	2.3487(4)
Ru(1)−N	2.108(6)	2.108(4)	2.096(5)	2.105(4)	2.099(2)
Ru(2)−N	2.066(6)	2.041(5)	2.020(9)	2.041(4)	2.029(2)
Ru(3)−N	2.108(6)	2.118(5)	2.096(5)	2.120(4)	2.111(2)
C≡N				1.108(7)	1.018(7)
				1.126(6)	1.028(6)
∢Ru(1)-Ru(2)-Ru(3)	171.15(4)	166.66(3)	172.7(6)	170.876(19)	180

[a] From reference [21]. [b] Ru(1) and Ru(3) are the terminal Ru^{2+} ions, and Ru(2) the central one.

band in the NIR region upon oxidation, whereas no bands are observed in this region for the neutral form.

To determine whether or not compound **2** is paramagnetic, we decided to examine the ^{1}H NMR spectra (Figure S2 in the Supporting Information). As expected for paramagnetic compounds, broadened peaks and large chemical shifts of resonance signals were observed. For the symmetrical structures of compound **2**, there should be only four peaks. Indeed, four lines with intensity ratios consistent with those expected (i.e., 1:1:1:1), centered at $\delta = 24.08$, 16.61, −18.91, and −22.10 ppm, were observed. According to MO analyses, the two-electron oxidized compound **3** should be diamagnetic. This is confirmed by the NMR spectrum, in which the peaks fall into the normal range for a diamagnetic compound. Four peaks appearing at $\delta = 9.22$, 7.78, 7.16, and 5.72 ppm are observed with the expected integration ratios. To obtain a clean spectrum of compound **1**, a slight excess of hydrazine was added to a solution of **2** in CD_2Cl_2 to generate **1** in situ. The spectrum of compound **1** also consists of four signals spanning a smaller range, which were found at $\delta =$ 9.09, 7.08, 6.58 and 6.47 ppm with the expected intensity ratios. The ^{1}H NMR spectra of these triruthenium compounds clearly show the symmetrical structures, the paramagnetism of compound **2**, and the diamagnetism of compounds **1** and **3**. The spectrum of compound **4** shows four signals at $\delta = 25.28$, 21.07, −22.01, and −27.53 ppm, and compound **5** has four signals at 39.04, 6.65, −25.78, and −51.83 ppm with the expected integration ratios. The data clearly show that compounds **4** and **5** are paramagnetic and their magnetic properties are quite different from each other.

Our previous magnetic measurements showed the diamagnetism of compound **1**.[21] Based on the theoretical calculations,[21,24] compound **2** has an unpaired electron. The measured μ_{eff} values are essentially constant between 10 and 300 K, but drop slightly at higher temperatures (Figure 4). The effective magnetic moment of 1.65 μ_B at 300 K indicates that the compound is paramagnetic with an unpaired electron, although the value is a little below that expected. The values of μ_{eff} for compounds **4** and **5** are measured to be 2.76 and 3.58 μ_B at 300 K, which correspond to the triplet state and the quartet spin state, respectively (Figures S3 and S4 in the Supporting Information).

Table 2. Crystal data for **2**, **3**, **4**, and **5**.

	2·2 CH_2Cl_2·$^1/_2H_2O$	**3**·6 CH_2Cl_2	**4**·2 CH_2Cl_2·H_2O	**5**·2 CH_2Cl_2·2 CCl_4
formula	$C_{42}H_{37}BCl_6F_4N_{12}O_{0.5}Ru_3$	$C_{46}H_{44}B_2Cl_{14}F_8N_{12}Ru_3$	$C_{44}H_{38}Cl_4N_{14}ORu_3$	$C_{46}H_{36}BCl_{12}F_4N_{14}Ru_3$
M_r	1320.56	1738.06	1223.89	1600.31
T [K]	150 (1)	150 (1)	150(1)	150(1)
diffractometer	NONIUS, Kappa CCD	BRUKER, SMART ApexCCD	NONIUS, Kappa CCD	BRUKER, SMART ApexCCD
λ [Å]	0.71073	0.71073	0.71073	0.71073
crystal system	monoclinic	orthorhombic	triclinic	monoclinic
space group	$P2_1/n$	$Fddd$	$P\bar{1}$	$C2/c$
a [Å]	11.3742 (1)	12.2606 (4)	12.0467(1)	15.3511(6)
b [Å]	20.9329(2)	21.7050 (7)	12.9793(1)	24.5627(9)
c [Å]	20.3272 (2)	48.3825 (15)	15.0324(2)	15.2503(6)
α [°]	90	90	91.6438(4)	90
β [°]	93.2781 (4)	90	90.0117(4)	90.282(1)
γ [°]	90	90	104.4230(6)	90
V [Å^3]	4831.89 (8)	12875.4 (7)	2275.35(4)	5750.3(4)
Z	4	8	2	4
μ [mm^{-1}]	1.321	1.344	1.272	1.398
crystal size [mm]	0.5×0.4×0.12	0.50×0.12×0.05	0.50×0.15×0.03	0.30×0.30×0.05
θ range [°]	1.40–27.50	1.68–27.50	1.36–27.50	1.56–27.50
reflections collected	32782	25801	49209	37625
independent reflections	11070 (R_{int} = 0.0615)	3708 (R_{int} = 0.0868)	10445 (R_{int} = 0.0690)	6604 (R_{int} = 0.0368)
R_F/R_{wF^2} (all data)[a]	0.0925/0.1577	0.0989/0.1830	0.0845/0.1335	0.0410/0.1009
R_F/R_{wF^2} [$I > 2\sigma(I)$][a]	0.0537/0.1339	0.0706/0.1679	0.0489/0.1114	0.0350/0.0969
GOF	1.043	1.062	1.103	1.096

[a] $R_F = \Sigma | F_o - F_c | / \Sigma | F_o |$; $R_{wF^2} = [\Sigma w | F_o^2 - F_c^2 |^2 / \Sigma w F_o^4]^{1/2}$.

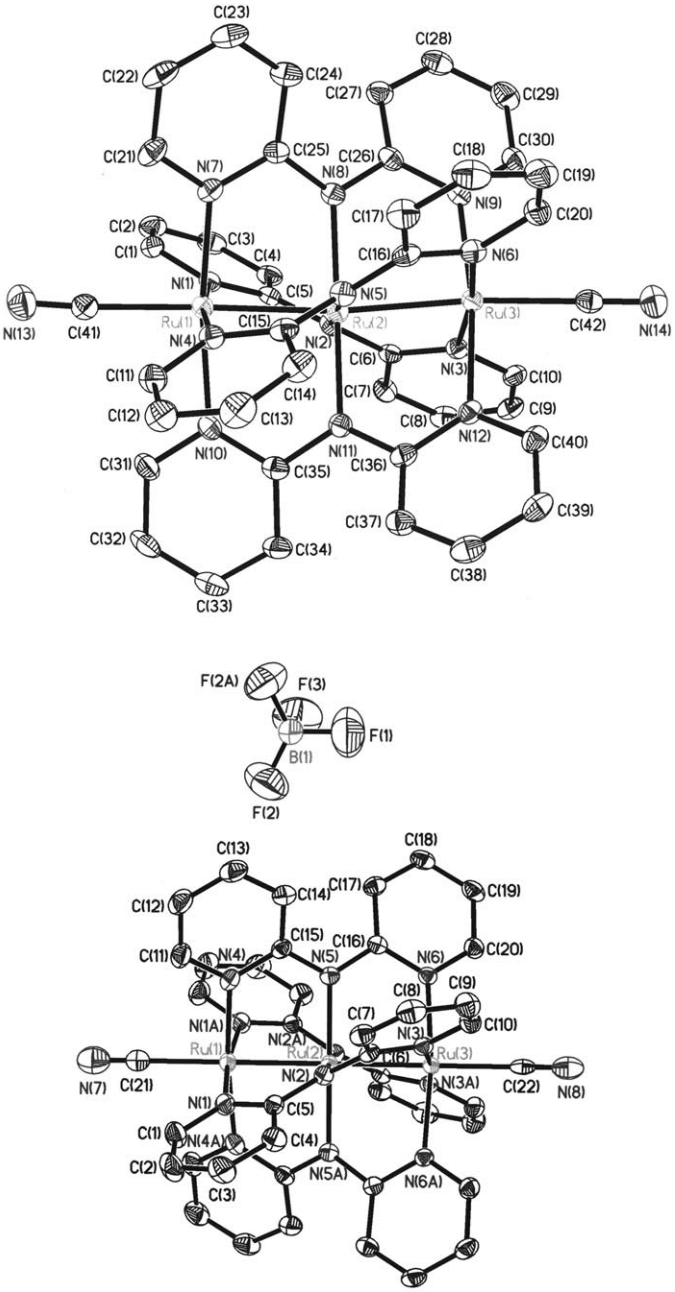

Figure 2. Crystal structures of **4** (top) and **5** (bottom). Atoms are drawn at the 30% probability level and hydrogen atoms are omitted for clarity.

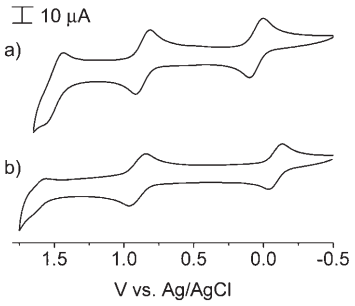

Figure 3. The cyclic voltammograms of a) **2** and b) **5** in CH_2Cl_2 containing 0.1 M TBAP.

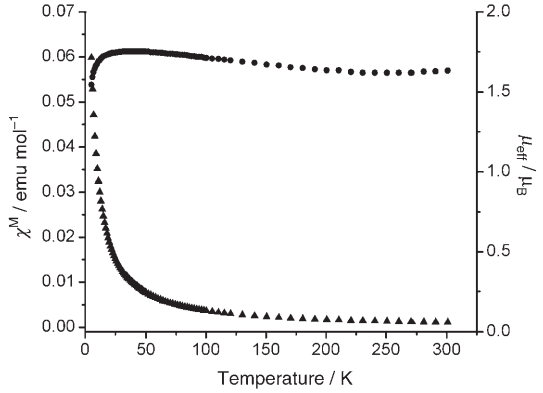

Figure 4. Temperature-dependent magnetic effective moment (●) and molar magnetic susceptibility (▲) for **2**.

To obtain further insight into the electronic structure of these compounds, a series of DFT calculations was performed. The geometries of compounds **1** and **4** were optimized in the idealized D_4 symmetry on the singlet state for compound **1** and the triplet state for compound **4**. The z axis is assumed collinear with the X–Ru_3–X (X = Cl; CN) axis. Some relevant geometrical parameters and results from DFT calculations are listed in Table 3. The optimized geometrical parameters are in good agreement with the experimental data, except that the Ru–C and C≡N distances of compound **4** are different from the experimental data. The geometry optimization for compound **4** with a fixed Ru–C distance (2.058 Å) was also carried out (Table 3). A comparison of the molecular orbitals of both calculations shows that the electronic configurations are similar. However, the optimized C≡N distances are still shorter than experimental results (Table 3). This suggests that the difference in Ru–C and C≡N bonds might be attributed to crystal packing forces and positional average effects.

Table 3. Relevant geometrical parameters[a] and results computed for $[Ru_3(dpa)_4(X)_2]$ (X = Cl, CN) in D_4 symmetry.

	X = Cl	X = CN	X = CN[b]
distances			
Ru–Ru	2.267	2.388	2.386
Ru–X	2.605	1.950	2.058
$Ru_{terminal}$–N	2.084	2.047	2.063
$Ru_{central}$–N	2.048	1.982	1.996
C–N	–	1.192	1.175
spin distribution[c]			
$Ru_{central}$	–	0.9840	0.9651
$Ru_{terminal}$	–	0.3082	0.3343

[a] Distances in Å. [b] Fixed Ru–C distances. [c] Spin distribution (number of electrons spin-α minus spin-β).

In a linear trimetal system, the d orbitals of the transition metals generate three types of molecular orbitals: 1) σ-type MOs (σ, σ_{nb}, and σ*), composed of d_{z^2} combinations. 2) π-type MOs (π, π_{nb}, and π*), composed of d_{xz} and d_{yz} orbitals.

3) δ-type MOs (δ, δ_{nb}, and δ*), composed of d_{xy} orbitals. These three types of MOs interact with different ligand group orbitals (LGOs) of the axial ligands. The difference in the electron configurations of compounds **1** and **4** may be caused by different types of trimetal–ligand bonding interactions: ligand-to-metal σ donation, ligand-to-metal π donation, and metal-to-ligand π back-bonding.

On the basis of structural analysis, the Ru–Ru distances of the $[Ru_3(dpa)_4Cl_2]$ (2.267 Å) are shorter than those of $[Ru_3(dpa)_4(CN)_2]$ (2.388 Å), that is, the Ru–Ru interaction of compound **1** is stronger than that of compound **4**. This stabilizes the σ and π bonding orbitals and destabilizes the σ* and π* antibonding orbitals. The Ru–Cl distances (2.605 Å) are much longer than Ru–CN (1.950 Å). This indicates that the interaction between Ru and Cl ions is weaker than that between Ru and CN ions. Thus, the σ_{nb} orbital (the antibonding interactions of the axial ligand with the trimetal chain) is destabilized in compound **4**. In addition to forming σ bonds, the CN ligand is capable of a π back-bonding interaction with the trimetal chain. The empty π* orbitals of the CN ligand interact with the π_{nb} and π* orbitals of the trimetal chain, thus the π_{nb} and π* orbitals are significantly lowered in energy. On the other hand, the Cl ligand can only form a π bonding interaction with the trimetal chain. The π* orbitals are slightly destabilized.

The computed molecular orbitals close to the Fermi level for compounds **1** and **4** are shown in Figure 5. The compositions of the most relevant molecular orbitals are shown in Figure 6 for compound **1** and Figure 7 for compound **4** as isosurfaces, corresponding to a value of the wavefunction ψ of 0.07 au. The LUMO ($40e_1$), HOMO ($22a_2$), and HOMO−1 ($18b_2$) of compound **1** can be classified as π*, σ_{nb}, and δ* orbitals, respectively, and the LUMO ($23a_2$), SOMO ($18b_2$), and SOMO−1 ($40e_1$) of compound **4** can be classified as the σ_{nb}, δ* and π* orbitals, respectively. The σ_{nb} orbitals of both compounds show an antibonding interaction with the axial ligands. The π* orbital of compound **1** shows significant metal character whereas the π* orbital of compound **4** exhibits a π back-bonding interaction with the axial CN ligand. The energy gaps between σ_{nb} and the other two orbitals for compound **4** are significantly larger than those for compound **1**. In contrast to compound **1** in which two electrons occupy the σ_{nb} orbital, there are two electrons occupied in the doubly degenerate π* orbitals for compound **4**.

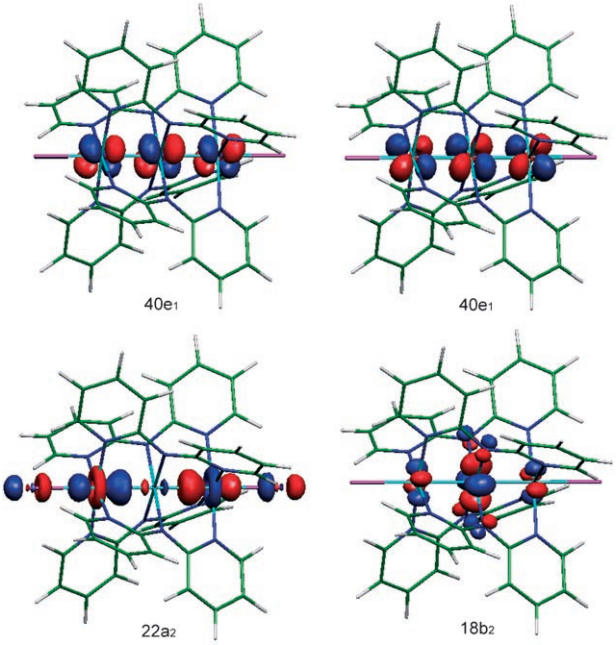

Figure 6. Molecular orbitals of **1** (the $40e_1$ MOs have two degenerate p sets, combinations of d_{xz} and d_{yz} orbitals).

Based on these DFT results and the previous report for building metal string molecular orbital diagrams,[24] the qualitative molecular orbital energy level correlation diagrams for compounds **1** and **4** were constructed and are shown in Figure 8. It should be noted that the interactions between δ-type orbitals of trimetal and axial ligands are weak. Therefore, these interactions are not discussed here. These qualitative MO diagrams are consistent with the DFT results (Figure 5). In compound **4**, the strong σ interactions between triruthenium and the axial CN ligands destabilize the σ_{nb} orbitals and π back-bonding interactions, with the axial CN ligand stabilizing the π* orbitals. These two orbitals are reversed in energy for compound **1**. Thus, the electronic configurations of these two compounds are different, that is, compound **1** is in the singlet state and compound **4** in the triplet state.

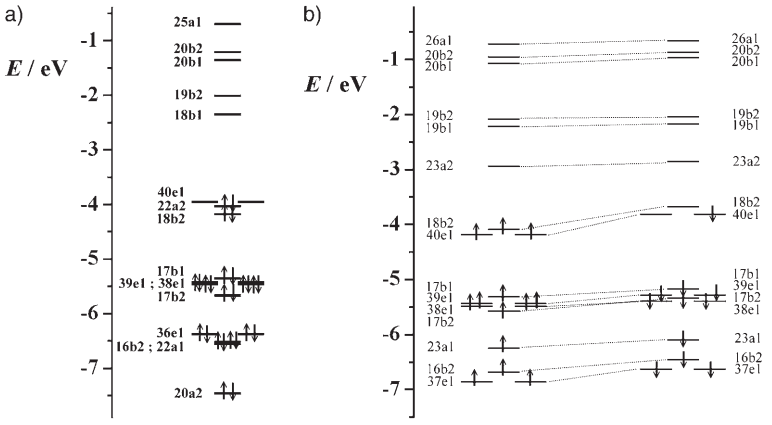

Figure 5. Molecular orbital diagrams for a) compound **1** from spin-restricted and b) compound **4** from spin-unrestricted calculations. In the spin-unrestricted calculation, the α and β counterparts of the molecular orbitals are connected with broken lines.

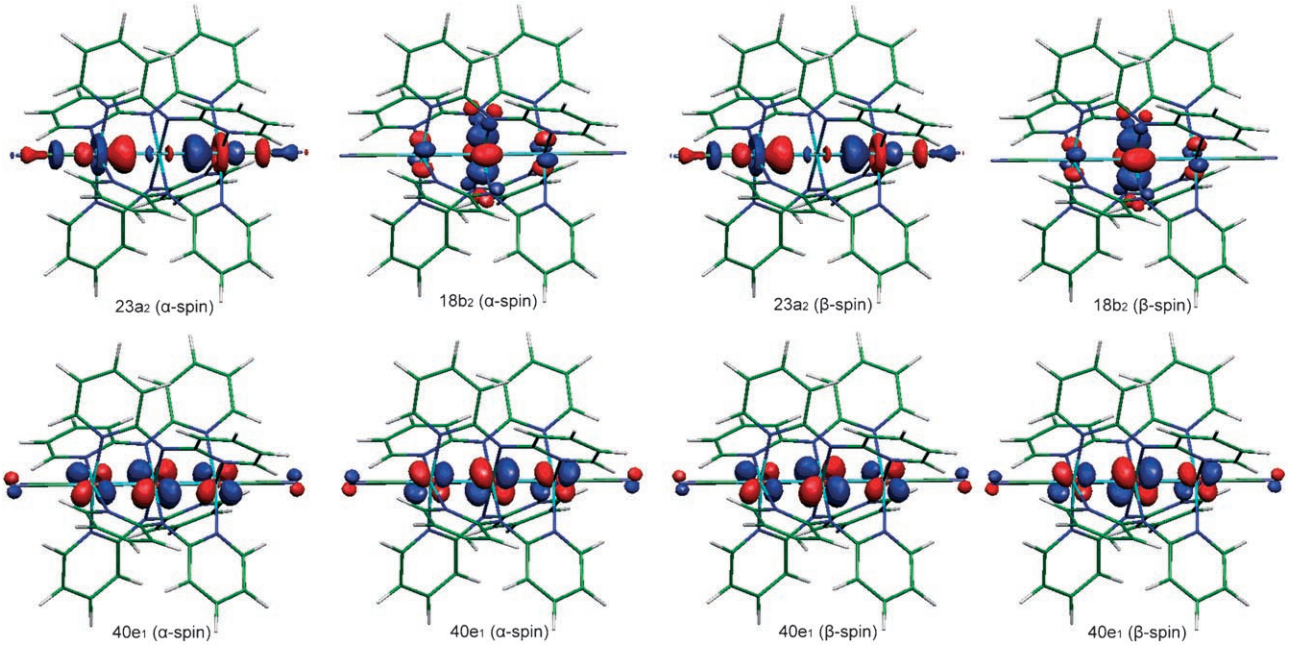

Figure 7. Molecular orbitals of **4** (the $40e_1$ MOs have two degenerate p sets, combinations of d_{xz} and d_{yz} orbitals).

Since there are two unpaired electrons in compound **4** it is essential to determine their locations. As listed in Table 3, the spin distribution values for compound **4** calculated by DFT are 0.9840 and 0.3082 for $Ru_{central}$ and $Ru_{terminal}$ ions, respectively. In a localized model, a spin value of 2 at $Ru_{central}$ is expected. The difference between the idealized value and calculated result can be attributed to the spin delocalization caused by the generalized gradient approximation (GGA) function[25] and the interaction of the Ru–Ru bond.

In addition to the larger spin distribution values on the $Ru_{central}$ ion, the contribution of the $Ru_{central}$ character in the two magnetic orbitals is also larger than that of the $Ru_{terminal}$ ion, as shown in Table 4. Thus, the two unpaired electrons occupy mainly the $Ru_{central}$ ion. Considering the $Ru_{central}$ ion of compound **1**, the interactions between four nitrogen atoms and the $Ru_{central}$ ion destabilize the $d_{x^2-y^2}$ orbital and the interactions between the $Ru_{central}$ and $Ru_{terminal}$ ions destabilize the d_{z^2} orbital. The six electrons of the $Ru_{central}$ ion occupy the three lower orbitals (d_{xy}, d_{yz}, and d_{xz}). Thus, the $Ru^{II}_{central}$ unit of compound **1** is in the singlet state as shown in Figure 9 (left). In the case of compound **4**, the weak interactions between the $Ru_{central}$ and $Ru_{terminal}$ ions stabilize the d_{z^2} orbital of the $Ru_{central}$ ion. The energy gap between the d_{z^2} and d_{xy} orbitals decreases and both the d_{xy} and d_{z^2} orbitals are singly occupied. The $Ru_{central}$ ion of compound **4** is in the triplet state as shown in Figure 9 (right). For the $Ru_{terminal}$ ions, the d_{z^2} and $d_{x^2-y^2}$ orbitals are destabilized due to the interactions with the axial ligand (Cl and CN). The $Ru_{terminal}$ ions of both compounds are in the d^6 low spin state ($S=0$).

DFT calculations were also performed on $[Ru_3(dpa)_4(CN)_2]^+$. The doublet and quartet electronic states were investigated and the relevant geometrical parameters and atomic spin distributions are listed in Table 5. The energy of the quartet state is significantly lower than that of the doublet state and the geometrical parameters are comparable to the experimental data. Therefore, the electronic configuration of compound **5** can be considered to be in the quartet state, consistent with the magnetic measurements.

The computed molecular orbital energy diagram for $[Ru_3(dpa)_4(CN)_2]^+$ is shown in Figure 10. The three unpaired electrons occupy the $18b_2$ (δ^*) and $40e_1$ (π^*) orbitals. The contribution of the $Ru_{central}$ character in these two magnetic orbitals is larger than that of the $Ru_{terminal}$ ion (Table 4). Moreover, the atomic spin value at $Ru_{central}$ (1.3051) is larger than that at $Ru_{terminal}$ (0.5632) for $[Ru_3(dpa)_4(CN)_2]^+$. It might be proposed that the $Ru_{central}$ atom is oxidized and has three unpaired electrons. The two electrons on the $40e_1$ orbitals are more or less delocalized over the Ru_3 unit through Ru–Ru bonds.

Conclusion

To summarize, the yield for the synthesis of linear triruthenium compounds has been improved under modified conditions. This allows us to obtain a large amount of material for further studies. In the crystal structures, the average Ru–Ru distance of the oxidized compounds is slightly longer than that of the neutral analogues. For compounds with chloride axial ligands, the Ru–Cl distance of the neutral compound is much longer than that of the oxidized compounds. Compounds **1–3** exhibit three reversible redox reactions, whereas compounds **4** and **5** show two reversible redox reactions. The electronic configuration changes significantly as the axial ligands are altered from chlorides to cyanides. The

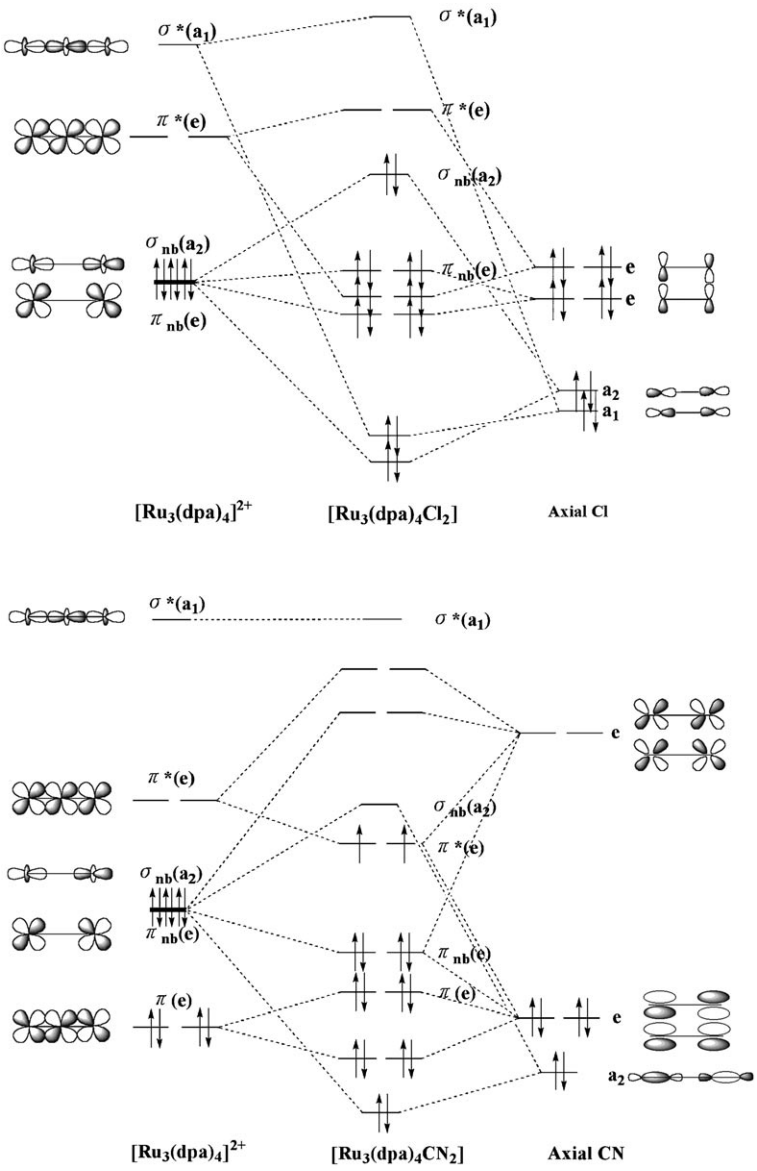

Figure 8. Qualitative molecular orbital energy level correlation diagrams for **1** (top) and **4** (bottom).

Table 4. The contribution of $Ru_{central}$ and $Ru_{terminal}$ character in the $40e_1$ and $18b_2$ orbitals of compounds **4** and **5**.

	$Ru_{central}$	$Ru_{terminal}$
$40e_1$ of **4**	43.35 %	41.66 %
$18b_2$ of **4**	32.37 %	11.46 %
$40e_1$ of **5**	46.21 %	36.01 %
$18b_2$ of **5**	26.54 %	19.54 %

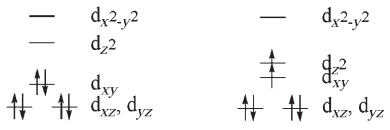

Figure 9. A schematic representation of $3d^6$ electronic configuration of isolated $Ru^{II}_{central}$ unit in **1** (left) and **4** (right).

magnetic measurements, ^1H NMR spectra, and crystal structures of these compounds are in agreement with the electronic structures obtained by theoretical calculations.

Experimental Section

General remarks: All reagents and solvents were obtained from commercial sources and were used without further purification unless otherwise noted. CH_2Cl_2 used for electrochemistry was dried over CaH_2 and freshly distilled prior to use. Tetra-*n*-butylammonium perchlorate (TBAP) was recrystallized twice from ethyl acetate and further dried under vacuum.

Physical measurements: Absorption spectra were recorded on Hewlett Packard model 8453 or JASCO V-570 spectrophotometers. IR spectra were obtained with a Nicolet Fourier-Transform IR spectrometer in the range of 500–4000 cm^{-1}. FAB-MS mass spectra were obtained with a JEOL HX-110 HF double focusing spectrometer operating in the positive ion detection mode. The molar magnetic susceptibility was recorded in the range of 5–300 K on a SQUID system with a 10000 Gauss external magnetic field. Electrochemistry was performed with a three-electrode potentiostat (CH Instruments, Model 750 A) in a CH_2Cl_2 deoxygenated by purging with prepurified nitrogen gas. Cyclic voltammetry was conducted with the use of a homemade three-electrode cell equipped with a BAS glassy carbon (0.07 cm^2) or platinum (0.02 cm^2) disk as the working electrode, a platinum wire as the auxiliary electrode, and a homemade Ag/AgCl (saturated) reference electrode. The reference electrode is separated from the bulk solution by a

Table 5. Relevant geometrical parameters[a] and results computed for $[Ru_3(dpa)_4(CN)_2]^+$ in D_4 symmetry.

	$S=3/2$	$S=1/2$
Ru–Ru	2.345	2.367
Ru–C	1.965	1.949
$Ru_{central}$–N	2.003	1.991
$Ru_{terminal}$–N	2.072	2.066
C–N	1.176	1.178
E [eV]	–	0.258
spin distribution[b]		
$Ru_{central}$	1.3051	0.5442
$Ru_{terminal}$	0.5632	0.3649

[a] Distances in Å. [b] Spin distribution (number of electrons spin-α minus spin-β).

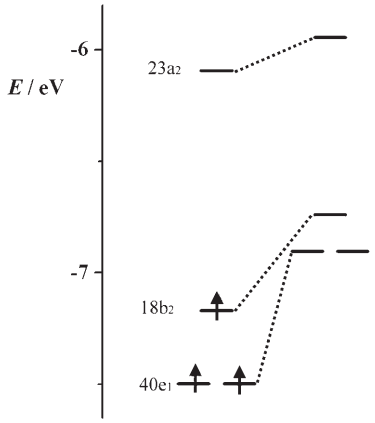

Figure 10. Molecular orbital diagrams for $[Ru_3(dpa)_4(CN)_2]^+$ from the spin-unrestricted calculation. In the spin-unrestricted calculation, the α and β counterparts of the molecular orbitals are connected with broken lines.

double junction filled with electrolyte solution. Potentials are reported versus Ag/AgCl (saturated) and referenced to the ferrocene/ferrocenium (Fc/Fc^+) couple which occurs at $E_{1/2} = +0.54$ V versus Ag/AgCl (saturated). The working electrode was polished with 0.03 μm alumina on Buehler felt pads and was subjected to ultrasound for 1 min prior to each experiment. The reproducibility of individual potential values was within ±5 mV. The spectroelectrochemical experiments were accomplished with the use of a 1 mm cuvette, a 100 mesh platinum gauze as working electrode, a platinum wire as auxiliary electrode, and a Ag/AgCl (saturated) reference electrode.

$[Ru_3(dpa)_4Cl_2]$ (1): Hydrazine (five drops) was added to a solution of compound **2** (114 mg, 0.1 mmol) in CH_2Cl_2 (100 mL). The mixture was stirred under a nitrogen atmosphere for 10 min, and then filtered through Celite. The solution was concentrated, layered by hexane, and crystallized at 4 °C to give 66 mg of dark brown crystals (63 %). IR (KBr): $\tilde{\nu}$ = 1597, 1587, 1541, 1458, 1420 cm^{-1} (py); UV/Vis (CH_2Cl_2): λ_{max} (ε) = 262 (9.59×10^4), 342 (5.80×10^4), 476 nm (1.01×10^4 $dm^3mol^{-1}cm^{-1}$); MS(FAB): *m/z*: 1055 $[Ru_3(dpa)_4Cl_2]^+$, 1020 $[Ru_3(dpa)_4Cl]^+$; elemental analysis calcd (%) for $[Ru_3(dpa)_4Cl_2]$: C 45.54, H 3.06, N 15.93; found: C 45.07, H 3.16, N 15.38.

$[Ru_3(dpa)_4Cl_2][BF_4]$ (2): Ligand dpaH (340 mg, 2.0 mmol), $Ru_2(OAc)_4Cl$ (710 mg, 1.5 mmol), LiCl (200 mg, 4.5 mmol), and naphthalene (20 g) were placed in an Erlenmeyer flask under an argon atmosphere. The mixture was refluxed gently for 30 min and then *tert*-butanol (10 mL) was added. The solution was refluxed for a further 10 min, then *tert*-BuOK (240 mg, 2.0 mmol) in *tert*-butanol (10 mL) was added,. The temperature was increased and the *tert*-butanol was slowly evaporated over a period of 30 min. The resulting solution was then stirred at 220 °C for an additional 90 min. After the mixture was cooled to 80 °C, hexane (100 mL) was added and the precipitate was filtered. The solid was extracted with CH_2Cl_2 (200 mL). Ferrocenium tetrafluoroborate (140 mg, 0.5 mmol) was added to the CH_2Cl_2 solution. The resulting solution was stirred for 10 min and then diethyl ether (100 mL) was added to precipitate the impurity. The mixture was filtered and the solvents were removed by a rotary evaporator. Crystallization from CH_2Cl_2 and diethyl ether afforded 302 mg of dark red crystals (53 %). IR (KBr): $\tilde{\nu}$ = 1604, 1469, 1457, 1424 cm^{-1} (py); UV/Vis (CH_2Cl_2): λ_{max} (ε) = 272 (9.76×10^4), 479 (6.66×10^3), 534 (5.95×10^3), 933 nm (6.76×10^3 $dm^3mol^{-1}cm^{-1}$); MS(FAB): *m/z*: 1055 $[Ru_3(dpa)_4Cl_2]^+$, 1020 $[Ru_3(dpa)_4Cl]^+$; elemental analysis calcd (%) for $[Ru_3(dpa)_4Cl_2][BF_4]$: C 42.08, H 2.83, N 14.72; found: C 41.88, H 2.86, N 14.41.

$[Ru_3(dpa)_4Cl_2][BF_4]_2$ (3): Excess $NOBF_4$ (60 mg, 0.5 mmol) was added to a solution of compound **2** (114 mg, 0.1 mmol) in CH_2Cl_2 (50 mL). The mixture was stirred at room temperature for 3 h, and then filtered. The solution was concentrated under reduced pressure. Crystallization from CH_2Cl_2 and diethyl ether produced 61 mg of dark purple crystals (50 %). IR (KBr): $\tilde{\nu}$ = 1599, 1552, 1460, 1422 cm^{-1} (py); UV/Vis(CH_2Cl_2): λ_{max} (ε) = 280 (9.66×10^4), 492 (5.89×10^3), 544 (6.34×10^3), 1054 nm (1.29×10^4 $dm^3mol^{-1}cm^{-1}$); MS(FAB): *m/z*: 1055 $[Ru_3(dpa)_4Cl_2]^+$, 1020 $[Ru_3(dpa)_4Cl]^+$; elemental analysis calcd (%) for $[Ru_3(dpa)_4Cl_2][BF_4]_2$: C 39.11, H 2.63, N 13.68; found: C 38.97, H 2.91, N 13.34.

$[Ru_3(dpa)_4(CN)_2]$ (4): Hydrazine (five drops) was added to a solution of compound **5** (50 mg, 0.04 mmol) in CH_2Cl_2 (50 mL). The mixture was stirred under a nitrogen atmosphere for 10 min, and then filtered through Celite. The solution was concentrated, layered by hexane, and crystallized at 4 °C to give 28.6 mg of dark brown crystals (62 %). IR (KBr): $\tilde{\nu}$ = 2058, 1613, 1467, 1421 cm^{-1} (py); UV/Vis (CH_2Cl_2): λ_{max} (ε) = 270 (6.58×10^4), 350 (3.52×10^4), 480 (5.80×10^3), 734 nm (3.49×10^3 $dm^3mol^{-1}cm^{-1}$); MS(FAB): *m/z*: 1037 $[Ru_3(dpa)_4(CN)_2]^+$, 1011 $[Ru_3(dpa)_4CN]^+$; elemental analysis calcd (%) for $[Ru_3(dpa)_4(CN)_2]$: C 45.54, H 3.06, N 15.93; found: C 45.07, H 3.16, N 15.38.

$[Ru_3(dpa)_4(CN)_2][BF_4]$ (5): Excess NaCN (65 mg, 1.3 mmol) was added to a solution of compound **2** (50 mg, 0.04 mmol) in CH_3CN (40 mL). The mixture was stirred at room temperature for 6 h, and then filtered. The solution was concentrated under reduced pressure. Crystallization from CH_2Cl_2 and CCl_4 produced 39.2 mg of dark purple crystals (80 %). IR (KBr): $\tilde{\nu}$ = 2049, 1609, 1465, 1420 cm^{-1} (py); UV/Vis(CH_2Cl_2): λ_{max} (ε) = 273 (1.27×10^5), 349 (5.85×10^4), 482 (8.50×10^3), 784 nm (1.21×10^4 $dm^3mol^{-1}cm^{-1}$); MS(FAB): *m/z*: 1037 $[Ru_3(dpa)_4(CN)_2]^+$, 1011 $[Ru_3(dpa)_4CN]^+$; elemental analysis calcd (%) for $[Ru_3(dpa)_4(CN)_2][BF_4]$: C 44.93, H 2.87, N 17.46; found: C 40.76, H 2.99, N 15.24.

X-ray crystallographic study: The chosen crystals were mounted on a glass fiber. Data collection was carried out on a NONIUS Kappa CCD diffractometer and a BRUKER SMART ApexCCD diffractometer with Mo radiation (λ = 0.71073 Å). Cell parameters were retrieved and refined using DENZO-SMN software on all observed reflections.[26] Data reduction was performed with the same software. An empirical absorption was based on the symmetry-equivalent reflections, and absorption corrections were applied with the SORTAV program.[27] All the structures were solved using SHELXS-97[28] and refined with SHELXL-97[29] by full-matrix least-squares methods on F^2 values. Hydrogen atoms were fixed at calculated positions and refined using a riding mode. The detailed crystal data are listed in Table 2. CCDC–618738–618741 (**2**, **3**, **4**, and **5**) contain the supplementary crystallographic data for this paper. These data can be obtained free of charge from The Cambridge Crystallographic Data Centre via www.ccdc.cam.ac.uk/data_request/cif.

Computational methods: All calculations and geometry optimizations reported in this article were carried out by using density functional theory (DFT) methods[30] with the ADF 2002.02 program package.[31] The local spin density (LSD) exchange correlation potential[30] was used with the local density approximation (LDA) of the correlation energy (Vosko, Wilk, Nusair).[32] Becke's nonlocal corrections[33] to the exchange energy and Perdew's nonlocal corrections[34] to the correlation energy were used. The scalar relativistic zero-order regular approximation (ZORA) was used within the ADF study.

Within the ADF program slater type orbitals (STO) with the following basis sets were used: double-ζ quality for H, double-ζ quality with polarization function for C, N, Cl and triple-ζ quality with polarization function for Ru. The inner shells were treated within the frozen-core approximation (1s for C and N, 1s–2p for Cl, 1s–3d for Ru).

Full geometry optimizations were carried out within the idealized D_4 symmetry constraints for $[Ru_3(dpa)_4Cl_2]$, $[Ru_3(dpa)_4(CN)_2]$, and $[Ru_3(dpa)_4(CN)_2]^+$. The spin-restricted formalism was used for the closed-shell ground state $[Ru_3(dpa)_4Cl_2]$, and the spin-unrestricted formalism was used for the open-shell ground state $[Ru_3(dpa)_4(CN)_2]$ and $[Ru_3(dpa)_4(CN)_2]^+$.

Acknowledgements

The authors acknowledge the National Science Council and the Ministry of Education of Taiwan for financial support. This work was supported by the National Center for High-Performance Computing.

[1] S. Aduldecha, B. Hathaway, *J. Chem. Soc. Dalton Trans.* **1991**, 993.
[2] G. J. Pyrka, M. El-Mekki, A. A. Pinkerton, *J. Chem. Soc. Chem. Commun.* **1991**, 84.
[3] L.-P. Wu, P. Field, T. Morrissey, C. Murphy, P. Nagle, B. Hathaway, C. Simmons, P. Thornton, *J. Chem. Soc. Dalton Trans.* **1990**, 3835.
[4] R. Clérac, F. A. Cotton, L. M. Daniels, K. R. Dunbar, C. A. Murillo, X. Wang, *J. Am. Chem. Soc.* **2001**, *123*, 1256.
[5] R. Clérac, F. A. Cotton, L. M. Daniels, K. R. Dunbar, T. Lu, C. A. Murillo, X. Wang, *J. Am. Chem. Soc.* **2000**, *122*, 2272.
[6] F. A. Cotton, L. M. Daniels, C. A. Murillo and I. Pascual, *J. Am. Chem. Soc.* **1997**, *119*, 10223.
[7] E.-C. Yang, M.-C. Cheng, M.-S. Tsai, S.-M. Peng, *J. Chem. Soc. Chem. Commun.* **1994**, 2377.
[8] F. A. Cotton, L. M. Daniels, G. T. Jordan IV, *Chem. Commun.* **1997**, 421.
[9] R. Clérac, F. A. Cotton, L. M. Daniels, K. R. Dunbar, K. Kirschbaum, C. A. Murillo, A. A. Pinkerton, A. J. Schultz, X. Wang, *J. Am. Chem. Soc.* **2000**, *122*, 6226.
[10] F. A. Cotton, C. A. Murillo, X. Wang, *Inorg. Chem.* **1999**, *38*, 6294.
[11] F. A. Cotton, L. M. Daniels, G. T. Jordan IV, C. A. Murillo, *J. Am. Chem. Soc.* **1997**, *119*, 10377.
[12] R. Clérac, F. A. Cotton, K. R. Dunbar, C. A. Murillo, I. Pascual, X. Wang, *Inorg. Chem.* **1999**, *38*, 2655.
[13] H.-C. Chang, J.-T. Li, C.-C. Wang, T.-W. Lin, H.-C. Lee, G.-H. Lee, S.-M. Peng, *Eur. J. Inorg. Chem.* **1999**, 1243.
[14] F. A. Cotton, L. M. Daniels, C. A. Murillo, X. Wang, *Chem. Commun.* **1999**, 2461.
[15] a) S.-J. Shieh, C.-C. Chou, G.-H. Lee, C.-C. Wang, S.-M. Peng, *Angew. Chem.* **1997**, *109*, 57; *Angew. Chem. Int. Ed. Engl.* **1997**, *36*, 56; b) C.-Y. Yeh, C.-H. Chou, K.-C. Pan, C.-C. Wang, G.-H. Lee, Y.-O. Su, S.-M. Peng, *J. Chem. Soc. Dalton Trans.* **2002**, 2670.
[16] C.-C. Wang, W.-C. Lo, C.-C. Chou, G.-H. Lee, J.-M. Chen, S.-M. Peng, *Inorg. Chem.* **1998**, *37*, 4059.
[17] Y.-H. Chen, C.-C. Lee, C.-C. Wang, G.-H. Lee, S.-Y. Lai, F.-Y. Li, C.-Y. Mou, S.-M. Peng, *Chem. Commun.* **1999**, 1667.
[18] S.-Y. Lai, T.-W. Lin, Y.-H. Chen, C.-C. Wang, G.-H. Lee, M.-H. Yang, M.-K. Leung, S.-M. Peng, *J. Am. Chem. Soc.* **1999**, *121*, 250.
[19] S.-Y. Lai, C.-C. Wang, Y.-H. Chen, C.-C. Lee, Y.-H. Liu, S.-M. Peng, *J. Chin. Chem. Soc.* **1999**, *46*, 477.
[20] S.-M. Peng, C.-C. Wang, Y.-L. Jang, Y.-H. Chen, F.-Y. Li, C.-Y. Mou, M.-K. Leung, *J. Magn. Magn. Mater.* **2000**, *209*, 80.
[21] J.-T. Sheu, C.-C. Lin, I. Chao, C.-C. Wang, S.-M. Peng, *Chem. Commun.* **1996**, 315.
[22] B. J. Coe, T. J. Meyer, P. S. White, *Inorg. Chem.* **1995**, *34*, 3600.
[23] J. L. Bear, B. Han, S. Huang, K. M. Kadish, *Inorg. Chem.* **1996**, *35*, 3012.
[24] J. F. Berry, F. A. Cotton, L. M. Daniels, C. A. Murillo, X. Wang, *Inorg. Chem.* **2003**, *42*, 2418.
[25] P. Kiehl, M.-M. Rohmer, M. Benard, *Inorg. Chem.* **2004**, *43*, 3151.
[26] "Macromolecular Crystallography, Part A: Processing of X-ray Diffraction Data Collected in Oscillation Mode": Z. Otwinowski, W. Minor, *Methods Enzymol.* **1997**, *276*, 307–326.
[27] R. H. Blessing, *Acta. Crystallogr. Sect. A* **1995**, *51*, 33.
[28] G. M. Sheldrick, *Acta. Crystallogr. Sect. A.* **1990**, *46*, 467.
[29] G. M. Sheldrick, SHELXL-97, Program for the Refinement of Crystal Structures, University of Göttingen (Germany), **1997**.
[30] R. G. Parr, W. Yang, *Density Functional Theory of Atoms and Molecules*, Oxford University Press, New York, **1989**.
[31] a) Amsterdam Density Functional (ADF), release 2002.02, Scientific Computing and Modelling, Theoretical Chemistry, Vrije Universiteit, Amsterdam, **2002**; b) E. J. Baerends, D. E. Ellis, P. Ros, *Chem. Phys.* **1973**, *2*, 41; L. Versluius, T. Ziegler, *J. Chem. Phys.* **1988**, *322*, 88; c) G. te Velde, E. J. Baerends, *J. Comput. Phys.* **1992**, *99*, 84; C. Fonseca Guerra, J. G. Snijders, G. te Velde, E. J. Baerends, *Theor. Chem. Acc.* **1998**, *99*, 391.
[32] S. H. Vosko, L. Wilk, M. Nusair, *Can. J. Phys.* **1980**, *58*, 1200.
[33] A. D. Becke, *Phys. Rev. A* **1988**, *38*, 3098.
[34] J. P. Perdew, *Phys. Rev. B* **1986**, *33*, 8822.

Received: August 24, 2006
Published online: November 29, 2006

